JCI The Journal of Clinical Investigation

ER stress upregulates S100A11 in steatohepatitis models via epigenetic modifications within the lipotoxicity influenced enhancer

P. Vineeth Daniel, … , Alexander Revzin, Harmeet Malhi

J Clin Invest. 2025. https://doi.org/10.1172/JCI191074.

Research In-Press Preview **Hepatology** **Inflammation** **Metabolism**

Metabolic dysfunction-associated steatohepatitis (MASH) is a progressive liver disease characterized by complex interactions between lipotoxicity, ER stress responses, and immune-mediated inflammation. We identified enrichment of the proinflammatory alarmin S100 calcium-binding protein A11 (S100A11) on extracellular vesicles stimulated by palmitate-induced lipotoxic ER stress with concomitant upregulation of hepatocellular S100A11 abundance in an IRE1A-XBP1s dependent manner. We next investigated the epigenetic mechanisms that regulate this stress response. Publicly available human liver ChIP-Seq GEO datasets demonstrated a region of histone H3 lysine 27 (H3K27) acetylation upstream to the *S100A11* promoter. H3K27acetylation ChIP-qPCR demonstrated a positive correlation between lipotoxic ER stress and H3K27acetylation of the region, which we termed Lipotoxicity Influenced Enhancer (LIE) domain. CRISPR-mediated repression of the LIE domain reduced palmitate-induced H3K27acetylation and corresponding *S100A11* upregulation in Huh7 cells and immortalized mouse hepatocytes. Silencing of the murine LIE in two independent steatohepatitis models demonstrated reduced S100a11 upregulation and attenuated liver injury. We confirmed H3K27acetylation and XBP1s occupancy at the LIE domain in human MASH liver samples and an increase in hepatocyte-derived S100A11-enriched extracellular vesicles in MASH patient plasma. Our studies demonstrate a LIE domain which mediates hepatic S100A11 upregulation. This pathway may be a potential therapeutic target in MASH.

ER stress upregulates S100A11 in steatohepatitis models via epigenetic modifications within the lipotoxicity influenced enhancer

P. Vineeth Daniel[1,#], Hanna L. Erickson[1], Daheui Choi[2], Feda H. Hamdan[1], Yasuhiko Nakao[1], Gyanendra Puri[1], Takahito Nishihara[1], Yeriel Yoon[1], Amy S. Mauer[1], Debanjali Dasgupta[1], Jill Thompson[3], Alexander Revzin[2], Harmeet Malhi[1]*

[1]Division of Gastroenterology and Hepatology, Mayo Clinic, Rochester, Minnesota, USA. [2]Department of Physiology and Biomedical Engineering, Mayo Clinic, Rochester, Minnesota, USA. [3]Department of Molecular Medicine, Mayo Clinic, Rochester, Minnesota, USA. [#]Present: Division of Medical Research, SRM Medical College Hospital and Research Centre, SRM Institute of Science and Technology, Kattankulathur, Chengalpattu, Tamil Nadu, India.

Corresponding author: Harmeet Malhi, M.B.B.S.
Professor of Medicine and Physiology
Mayo Clinic
200 First Street SW, Rochester, Minnesota 55905
Tel: 507 284 0686; Fax: 507 284 0762
Malhi.harmeet@mayo.edu

Conflict of interest statement: The authors declare that no conflict of interest exists.

Word count: 10,800 (title page, main text, references, figure legends, and tables)
Figures: 5; Supplementary figures: 9
Supplementary tables: 3
References: 57

ABBREVIATIONS

Ac: Acetylation

ASGR1: Asialoglycoprotein Receptor 1

ASGR2: Asialoglycoprotein Receptor 2

ATF6a: Activating Transcription Factor 6 alpha

CDAHFD: Choline-Deficient, L-Amino Acid-Defined High-Fat Diet

DAMP : Damage Associated Molecular Pattern

dCas9-KRAB: deactivated Cas9 - Kruppel Associated Box

EV: Extracellular Vesicle

FFC: High-Fat -Fructose and -Cholesterol

HAT: Histone Acetyltransferase

H3K27: Histone H3 lysine 27

HMGB1: High Mobility Group Box 1

IRE1A: Inositol Requiring Enzyme 1 Alpha

IMH: Immortalized Mouse Hepatocyte

LIE: Lipotoxicity Influenced Enhancer

MASH: Metabolic Dysfunction-associated Steatohepatitis

PA: Palmitic Acid/Palmitate

PERK: Protein Kinase R like ER Kinase

PMH: Primary Mouse Hepatocyte

SPR: Surface Plasmon Resonance

TSS: Transcription Start Site

UPR: Unfolded Protein Response

ABSTRACT

Metabolic dysfunction-associated steatohepatitis (MASH) is a progressive liver disease characterized by complex interactions between lipotoxicity, ER stress responses, and immune-mediated inflammation. We identified enrichment of the proinflammatory alarmin S100 calcium-binding protein A11 (S100A11) on extracellular vesicles stimulated by palmitate-induced lipotoxic ER stress with concomitant upregulation of hepatocellular S100A11 abundance in an IRE1A-XBP1s dependent manner. We next investigated the epigenetic mechanisms that regulate this stress response. Publicly available human liver ChIP-Seq GEO datasets demonstrated a region of histone H3 lysine 27 (H3K27) acetylation upstream to the *S100A11* promoter. H3K27acetylation ChIP-qPCR demonstrated a positive correlation between lipotoxic ER stress and H3K27acetylation of the region, which we termed Lipotoxicity Influenced Enhancer (LIE) domain. CRISPR-mediated repression of the LIE domain reduced palmitate-induced H3K27acetylation and corresponding S100A11 upregulation in Huh7 cells and immortalized mouse hepatocytes. Silencing of the murine LIE in two independent steatohepatitis models demonstrated reduced *S100a11* upregulation and attenuated liver injury. We confirmed H3K27acetylation and XBP1s occupancy at the LIE domain in human MASH liver samples and an increase in hepatocyte-derived S100A11-enriched extracellular vesicles in MASH patient plasma. Our studies demonstrate a LIE domain which mediates hepatic S100A11 upregulation. This pathway may be a potential therapeutic target in MASH.

Keywords: Unfolded protein response, Alarmin, Inflammation, Fatty Liver, Lipid Metabolism.

INTRODUCTION

Metabolic dysfunction-associated steatohepatitis (MASH) is the most prevalent chronic liver disease worldwide. MASH involves the accumulation of lipids, termed steatosis, along with inflammation and liver damage, known as lipotoxicity. Damaged liver cells release soluble mediators like damage associated molecular patterns (DAMPs) or alarmins that stimulate a localized chronic sterile inflammatory response (1, 2). Alarmin proteins execute dual functions: maintaining cellular homeostasis while also activating inflammatory mechanisms in response to tissue damage signals. High mobility group box 1, IL-1 alpha, IL-33, and the S100 family of proteins are well-reported alarmin proteins (3). Both parenchymal and non-parenchymal liver cells sense alarmins via pattern recognition receptors leading to the infiltration of pro-inflammatory systemic immune cells into the liver. In brief, hepatic lipotoxicity serves as a critical metabolic stressor that stimulates inflammation in the liver via the release of alarmin proteins (4).

ER stress is a well-established feature of lipotoxicity in MASH (5). Lipotoxic ER stress-induced cell dysfunction and lipoapoptosis are associated with sterile inflammation in the liver (6). Recently, we have reported the release of inflammatory DAMP-containing extracellular vesicles (EVs) from lipotoxic hepatocytes (7, 8). EVs are cell-specific membranous nanovesicles that feature differential cargo and composition under stress conditions imparting stress- and tissue-specific characteristics (9). In this context, our lab has previously demonstrated that lipotoxic ER stress mediates EV release from hepatocytes in an inositol requiring enzyme 1 alpha (IRE1A)-dependent manner (10). Additionally, we have reported that ceramide-dependent lipotoxic EVs are enriched with DAMPs (11). Given that MASH is inherently lipotoxic and exhibits elevated intrahepatic inflammatory signaling, we anticipated that lipotoxic EV cargos may be a pathogenically relevant pool of candidate proteins in MASH.

The susceptibility and variability of MASH progression and response to therapeutic agents can vary substantially across individuals. The unpredictable rate of MASH progression suggests genetic or epigenetic factors may explain individual variability. While GWAS and population genetics highlight genetic variants that could promote the onset or progression of MASH, there is limited knowledge of the epigenetic determinants of disease progression, which has emerged as a key mechanism that could explain the impact of dynamic and non-genetic factors on MASH progression (12, 13). Epigenetic mechanisms can regulate the transcriptomic perturbations elicited by lipotoxicity (14). A few studies have demonstrated an association of epigenetic changes with MASH, identifying high calorie diet as having remodeled the DNA methylome subsequently leading to hepatic steatosis (15, 16). However, the molecular mechanisms of epigenetic regulators like histone code and DNA methylation, microRNAs, and long non-coding RNAs in MASH pathogenesis and progression are not well understood (14, 17). Since epigenetic regulation demonstrates cell- and stimulus-specificity (18), similar to the ER stress response, a crosstalk between lipotoxic ER stress and epigenetic mechanisms may determine critical characteristics of MASH.

Integrating hepatocyte EV alarmins with individual variability, we asked whether a lipotoxic ER stress-dependent epigenetically regulated alarmin may modulate liver inflammation in MASH. Here, we report that lipotoxic ER stress upregulated S100 calcium-binding protein A11 (S100A11) expression, both within the cytosolic and EV pool, in an IRE1A-spliced X-box binding protein 1 (XBP1s)-dependent manner. Additionally, we observed that lipotoxic ER stress stimulates an epigenetic response by histone H3 lysine 27 (H3K27) acetylation (ac) of an enhancer element upstream to the *S100A11* promoter. CRISPR interference (CRISPRi)-mediated repression of this transcriptional complex lowered hepatic *S100a11* expression and mitigated steatohepatitis

in murine MASH models. We additionally confirmed that this epigenetic regulation is observed in human MASH livers. Overall, our study identifies S100A11 as a hepatocyte lipotoxicity-specific druggable target, regulated by a functional Lipotoxicity Influenced Enhancer (LIE) DNA element, which may explain individual variability in MASH.

RESULTS

S100A11 is enriched in hepatic lipotoxic EVs. To investigate DAMPs enriched in secreted EVs of lipotoxic hepatocytes, we utilized EV-proteomics as previously published by us (11). We treated an immortalized, non-transformed, wildtype hepatocyte cell line, termed immortalized mouse hepatocytes (WT-IMH) (11, 19, 20) with palmitate or vehicle and isolated EVs by differential ultracentrifugation of cell culture supernatants followed by untargeted proteomics (Figure 1A). Bioinformatic analysis of the reads yielded 1660 proteins to be differentially expressed, as shown in the volcano plot (Figure 1B). Focusing on DAMPs (21), we observed 44 proteins to be differentially expressed, among which S100A11 was upregulated, supporting our previous finding of S100A11 abundance as a ceramide-dependent EV cargo (11). Among the S100 family of proteins, S100A6 and S100A10 were also differentially expressed, albeit to a lower fold than S100A11 (Figure 1B) (3, 22).

We next evaluated S100A11 expression on EVs using a combination of qualitative and quantitative methods including electron microscopy (EM), surface plasmon resonance (SPR), western blotting (WB), and ELISA. Using immuno-gold EM and antibodies against S100A11, we observed an increase in S100A11 on the surface of palmitate-stimulated primary mouse hepatocyte (PMH)-derived EVs (Figure 1C) compared to the vehicle group (23). To quantify S100A11 abundance on EVs, we employed an SPR and antibody-based detection method. In this approach (Supplemental Figure 1A), $2x10^9$ EVs collected from palmitate or vehicle treated PMHs were infused into the SPR instrument, wherein EVs were captured on an SPR chip functionalized with an asialoglycoprotein receptor 1 (ASGR1) antibody, a hepatocyte specific marker (24). Next, the S100A11 signals on the captured EVs were quantified using SPR and anti-S100A11 antibody. We observed that EVs isolated from the palmitate-stimulated PMHs had enrichment of S100A11

signals compared to the vehicle treated PMHs (Figure 1D). To confirm EV enrichment of S100A11 in a human cell line, Huh7 cells were treated with palmitate. Western blotting of the EV lysates demonstrated increased S100A11 expression in EVs isolated from palmitate-treated Huh7 cells (Supplemental Figure 1B). Further, we measured S100A11 protein by ELISA in the Huh7-conditioned cell culture supernatants containing EVs and following EV depletion. Palmitate-treated Huh7 cell culture supernatants displayed higher S100A11 protein levels (Figure 1E). In cell culture supernatants depleted of EVs, there was no statistically significant difference in S100A11 levels between control and palmitate supernatants (Figure 1E). Yet, EVs isolated from these samples demonstrated an increase in S100A11 in palmitate-treated Huh7 EVs confirming the preferential secretion of S100A11 in EVs (Figure 1E). Thus, palmitate-induced lipotoxicity leads to the release of S100A11-enriched EVs.

Identification of S100A11 as an EV-bound DAMP secreted from lipotoxic hepatocytes made us question if MASH patient plasma samples also exhibited increased S100A11 on circulating hepatocyte-derived EVs. To answer this question, we measured hepatic S100A11 in EVs from plasma samples of MASH patients using SPR technique. EVs were isolated using differential ultracentrifugation. There was an increase in EVs in MASH plasma samples compared to the control plasma samples when quantified by Nanoparticle Tracking Analysis, consistent with our earlier data (Supplemental Figure 1C) (10). Asialoglycoprotein receptor 2 (ASGR2) expressing EVs, which are hepatocyte-derived (24, 25), were higher in MASH plasma samples compared to control samples (Figure 1F). Normalization of SPR signals based on EV numbers demonstrated equivalent EV capture amongst the two groups (Supplemental Figure 1D). Taken together, these data confirm that MASH plasma samples have increased numbers of hepatic EVs compared to the control. Labeling of captured EVs with an anti-S100A11 antibody revealed higher S100A11 SPR

signal for MASH samples compared to control samples with and without EV number normalization (Figure 1, G and H). Further labeling of the ASGR2-captured, S100A11-labelled EVs with anti-CYP2E1 antibody (a second independent hepatocyte specific marker), confirmed MASH samples to have increased S100A11 on dual (ASGR2 and CYP2E1) labeled hepatic EVs compared to the controls (Supplemental Figure 1E). Thus, these data demonstsrate hepatocyte-derived S100A11 is a highly upregulated lipotoxic EV cargo in MASH.

IRE1A regulates lipotoxic ER stress mediated S100A11 upregulation. Increased cellular expression of EV cargo proteins is one mechanism which can lead to their enrichment in EVs. Therefore, we asked if lipotoxic conditions stimulated the upregulation of S100A11 leading to its subsequent release on hepatocyte derived EVs. Assessment of the human MASH livers demonstrated upregulation of *S100A11* transcripts in MASH livers compared to control livers (Figure 2A). Palmitate-treated PMHs also exhibited upregulation of *S100a11* transcripts compared to vehicle treated controls (Figure 2B) consistent with previous studies in human MASH and free fatty acid treated hepatocyte cell lines (26, 27). To elucidate the hepatocellular signaling mechanisms that mediate transcriptional upregulation of S100A11 in lipotoxic conditions, we next employed Huh7 cells. Similarly to human MASH and palmitate-treated PMH cells, we noted that palmitate-treated Huh7 cells had enhanced *S100A11* mRNA expression, in comparison to the control (Figure 2C). Palmitate-treated Huh7 also had increased cytosolic S100A11 protein levels demonstrated by western blotting and densitometry (Figure 2, D and E).

Increased levels of circulating saturated free fatty acids in metabolic diseases like MASH are reported to activate the unfolded protein response (UPR) sensors by lipotoxic ER stress (8, 28, 29). Consistent with our previous observations (10), we observed palmitate stimulation to increase

190 *XBP1s* transcripts, indicative of activation of IRE1A (Supplemental Figure 2, A and B). Since
191 palmitate can also activate the other UPR sensors, protein kinase R-like ER kinase (PERK) and
192 activating transcription factor 6 alpha (ATF6α) (30), we asked which of these pathways may
193 regulate *S100A11*. We treated Huh7 cells with palmitate and specific pharmacological inhibitors
194 for each of the UPR sensors and measured *S100A11* transcripts. The palmitate-stimulated Huh7
195 cells had maximum repression of *S100A11* transcripts in the presence of the IRE1A RNase-specific
196 inhibitor (MKC8866) (Figure 2F), whereas PERK (GSK2606414) and ATF6α (Ceapin-A7)
197 inhibitors did not repress palmitate-induced *S100A11* upregulation (Supplemental Figure 2C). We
198 next employed a genetic approach, wherein we treated *Ire1a*$^{-/-}$ immortalized mouse hepatocytes
199 (IRE1A-KO-IMH) with palmitate and noted lack of upregulation of *S100a11* transcript levels
200 compared to WT-IMH controls (Supplemental Figure 2D). Thus, employing complementary
201 chemical and genetic approaches we confirmed that the transcriptional upregulation of *S100A11* is
202 IRE1A-dependent.

203 Correspondingly, mass spectrometric analysis of the proteomic composition of the EV's
204 collected from palmitate-stimulated IRE1A-KO-IMH (28) demonstrated S100A11 to be
205 downregulated (Figure 2G), reinforcing the role of IRE1A in S100A11 upregulation and
206 enrichment on lipotoxic EVs. To confirm these observations with a quantitative assay, we next
207 utilized SPR based measurement of S100A11 on EVs derived from palmitate and vehicle
208 stimulated WT-IMH and IRE1A-KO-IMH cells. Palmitate stimulation enriched S100A11
209 abundance on the EVs derived from WT-IMH cells, while palmitate stimulated IRE1A-KO-IMH
210 cells secreted EVs had lower levels of S100A11 (Figure 2H). Taken together, we inferred that
211 lipotoxic ER stress regulates *S100A11* transcription and EV enrichment downstream of IRE1A
212 signaling.

Palmitate-induced lipotoxic ER stress epigenetically orchestrates S100A11 transcription.

To understand how IRE1A regulates *S100A11,* we assessed the role of XBP1s, which is the active spliced isoform of a transcription factor that acts as a key downstream mediator of the IRE1A signaling axis. We found a putative XBP1s consensus site in the *S100A11* promoter upstream to the transcription start site (TSS) in Huh7 cells (Supplemental Figure 3A). We designed ChIP primers that spanned the consensus site to assess XBP1s occupancy on the promoter and performed ChIP assays. ChIP-qPCR demonstrated that palmitate stimulation in cell culture enriched XBP1s on the *S100A11* promoter relative to the isotype controls (Supplemental Figure 3B). We also assessed the human MASH livers by ChIP assay to verify XBP1s occupancy on the *S100A11* promoter. ChIP-qPCR demonstrated enrichment of XBP1s on the *S100A11* promoter in MASH livers compared to the control livers (Supplemental Figure 3C).

To investigate a functional, transcriptional outcome related to promoter occupancy, we employed a dual reporter-based promoter luciferase assay. We cloned the promoter sequence of human *S100A11* (Supplemental Figure 3D) containing the XBP1s consensus site (31) into a pGL4.22 vector and assessed *S100A11* promoter activity with co-transfection of TK-Renilla plasmid in Huh7 cells. We also included a substitution mutant of the XBP1s consensus site in the assay. Palmitate treatment increased *S100A11* promoter activity modestly, yet statistically significant, with respect to vehicle control (Supplemental Figure 3E). *S100A11* promoter mutant did not attenuate palmitate-induced *S100A11* promoter activity (Supplemental Figure 3E). Although we demonstrated the occupancy of XBP1s on the *S100A11* promoter by ChIP and activity in promoter reporter construct-based studies, the mutation studies suggested additional regulatory elements.

Transcription is regulated at multiple levels, including chromatin remodeling, promoter activity, and enhancer function, which control DNA accessibility and gene expression. XBP1s is reported to interact with a histone lysine acetyltransferase (HAT) p300 (32, 33), which is a chromatin-modifying enzyme that regulates gene transcription (34-36). Thus, we interrogated histone acetylation downstream of lipotoxic ER stress in regulating the transcription of *S100A11*. Since H3K27ac symbolizes an active mark on the distal regulating enhancer elements (37), we reviewed the genomic region around the *S100A11* gene using publicly available H3K27ac ChIP-Seq datasets. We identified a 1.2kb H3K27ac genomic region upstream of the TSS in Huh7 cells (Figure 3A), indicative of a putative enhancer element. We also noticed a similar H3K27ac domain within the same genomic coordinates in additional liver samples (Supplemental Figure 4A). In vitro analysis of this genomic region through ChIP qPCR demonstrated an increase in H3K27ac of the enhancer region in palmitate-treated cells (Figure 3B), which we termed "Lipotoxicity Influenced Enhancer" (LIE).

Enhancer-mediated transcriptional regulation requires close proximation of the transcription factor and enhancer element (38). We therefore performed a ChIP assay to assess XBP1s interaction with the LIE domain. ChIP qPCR analysis from palmitate-treated Huh7 cells showed increased enrichment of both XBP1s as well as p300 on the LIE domain (Figure 3, C and D) suggesting a functional co-regulatory complex. To validate our in vitro findings, we analyzed human MASH livers and normal liver samples through ChIP-qPCR. MASH liver samples demonstrated enrichment of H3K27ac on the LIE domain and concomitant abundance of XBP1s as well as p300 on the LIE domain compared to the normal livers (Figure 3, E-G). As additional proof, we simultaneously treated Huh7 cells with palmitate and A485, a p300 inhibitor, and noted repression of palmitate-induced *S100A11* transcriptional upregulation on inhibition of p300

(Supplemental Figure 4B). Collectively, our data confirms the *S100A11* transcriptional program to be a multi-partnered regulatory program comprising XBP1, p300, and the LIE domain (Supplemental Figure 4C).

To further establish biological relevance of the LIE element within palmitate-induced lipotoxicity, we utilized deactivated Cas9-Kruppel associated box (dCas9-KRAB)-mediated CRISPRi technology (Supplemental Figure 4D). In this method (39), the recruitment of the dCas9-KRAB fusion protein, guided by the sgRNA, leads to the repression of enhancer-mediated epigenetic regulation. We compared the putative H3K27ac mark across publicly available ChIP-Seq GEO-dataset for human hepatocyte and liver samples (Supplemental Figure 4A) and designed 2 sgRNAs targeting the LIE domain. We transiently transfected LIE specific sgRNAs into dCas9-KRAB-expressing Huh7 cell line (Supplemental Figure 4E) and stimulated the cells with palmitate. First, we assessed if the LIE sgRNAs exhibited enhancer silencing by performing H3K27ac ChIP-qPCR. We observed that transient transfection of LIE sgRNAs reduced palmitate-induced H3K27ac activation mark on the LIE domain (Supplemental Figure 4F). We next interrogated if LIE repression attenuated S100A11 transcription in lipotoxic hepatocytes. The LIE sgRNAs-transfected cells failed to induce *S100A11* mRNA levels with palmitate treatment, with reduced expression in comparison to the palmitate-treated controls (Figure 3H). Palmitate-mediated increase in cytosolic S100A11 protein abundance was also attenuated in LIE sgRNA-transfected cells with respect to the controls (Figure 3, I and J).

Since our EV-proteomics dataset had also identified S100A6 and S100A10 on lipotoxic EVs and several S100 family genes are clustered on the same chromosomal location (1q21.3 in humans and 3qF1-F2.1 in mice), we asked if LIE regulated *S100A6* and *S100A10* transcripts. qPCR analysis demonstrated LIE silencing did not affect the transcripts of *S100A6* and *S100A10*

downstream of palmitate-induced lipotoxic ER stress (Supplemental Figure 5, A and B). Palmitate is reported to regulate induced gene expression via hyperacetylation (40). Hence we asked if palmitate-induced hyperacetylation regulated *S100A11* transcription via LIE activation. Although we observed palmitate stimulation to increase cellular acetyl Co-A levels (Supplemental Figure 5C), repression of the LIE domain in palmitate stimulation demonstrated attenuated *S100A11* transcripts and protein levels. These observations confirmed palmitate-induced *S100A11* upregulation via increased H3K27ac of the LIE domain to be epigenetically regulated by XBP1s-p300 complex and not an outcome of palmitate-induced increase in acetyl Co-A levels. Taken together, we demonstrate that palmitate-induced lipotoxic ER stress mediates the transcriptional upregulation of *S100A11* via an epigenetically active enhancer, the LIE element.

In vivo repression of the murine hepatic LIE attenuates choline-deficient, L-amino acid-defined high-fat diet (CDAHFD)-induced steatohepatitis.

We next wanted to extend our observations of a functional LIE element from a cellular model of palmitate-induced lipotoxicity to a murine model of steatohepatitis. Therefore, we asked if repression of the LIE domain would attenuate hepatic S100A11 expression and thereby protect mice from developing MASH. To address this question, we reviewed publicly available H3K27ac ChIP-Seq datasets (Supplemental Figure 6A) from murine liver samples, to identify a mouse specific LIE domain. We noticed an active H3K27ac peak, upstream to the TSS of the murine *S100a11* gene. We designed sgRNAs spanning this murine LIE region and screened them using dCas9-KRAB expressing WT-IMH cells (Supplemental Figure 6B). We selected two sgRNA sequences that attenuated palmitate-induced *S100a11* upregulation (Supplemental Figure 6C) for subsequent in vivo studies. C57BL/6J mice, with endogenous expression of dCas9-KRAB (41)

were employed for this study. Homozygous expression of the *dCas9-KRAB* cassette was PCR verified (Supplemental Figure 6D). We next employed commercially generated viral vectors AAV8-LIE, which incorporated our validated sgRNAs, and AAV8-scr (Supplemental Figure 6E), for the murine studies.

Our initial approach adopted the relatively rapid CDAHFD model of MASH with classic histological, biochemical, and signaling features of steatohepatitis (42, 43). Mice were placed on the CDAHFD for 1 week following which mice received either AAV8-LIE or AAV8-scr viral vectors at a dose of $1x10^{12}$ genome copies/mouse (Figure 4A). Mice were maintained on their respective diets for an additional 2 weeks prior to analysis. Phenotypically, the AAV8-LIE or AAV8-scr injected, CDAHFD fed mice did not show a statistically significant difference in their body weight and liver to body weight ratios across the study groups (Supplemental Figure 7A). CDAHFD induced marked liver injury as measured by plasma levels of alanine transaminase (ALT) in AAV8-scr injected mice. The CDAHFD-LIE group had lower ALT values compared to the CDAHFD-scr controls in both male and female mice (Figure 4B). We measured the expression of *iCre* transcripts as a readout of viral transduction and expression efficiency. The *iCre* expression was comparable across all virally transduced liver samples within each group (Supplemental Figure 7B). Viral transduction of AAV8-LIE was also verified by PCR amplifying a small amplicon of the AAV8-LIE plasmid followed by sequencing from AAV8-LIE injected mouse livers (Supplemental Figure 7C). Concomitant with the ALTs, CDAHFD-scr mouse livers had higher *S100a11* transcript levels compared to the con-scr mice while CDAHFD-LIE mice had a attenuation of *S100a11* transcripts compared to the CDAHFD-scr controls (Figure 4C). To investigate non-specific effects of AAV8-LIE targeting, we assessed *S100a10* and *S100a13* genes as they were located close to the LIE domain and *Bip, Atf2, and Ager* genes as they were associated

with ER stress and S100A11 signaling. qPCR of the CDAHFD-fed mouse livers did not demonstrate a diet-induced increase in *S100a10* and *S100a13*, nor their repression (Supplemental Figure 7, D and E). Similar data were obtained for *BiP* and *Atf2* (Supplemental Figure 7, F and G). In contrast, *Ager* was induced by CDAHFD feeding, consistent with our prior studies (44), and was not repressed by AAV8-LIE (Supplemental Figure 7H). Thus, we did not observe non-specific silencing of other genes in proximity, candidate UPR genes, or *Ager*, which is known to be upregulated in MASH.

With an aim to assess macrophage accumulation within the hepatic parenchyma, we quantified *Mac2* transcripts. mRNA abundance of *Mac2* was increased in CDAHFD-scr mouse livers whereas CDAHFD-LIE had lower *Mac2* transcripts, suggesting a reduction in macrophage infiltration (Figure 4D). Correspondingly, H&E-stained liver sections demonstrated that CDAHFD-scr mouse livers developed steatosis and inflammation (Figure 4E). In contrast, CDAHFD-LIE mouse livers demonstrated no difference in steatosis but had fewer immune infiltrates (Supplemental Figure 7I) indicating murine LIE repression reduces inflammatory cell accumulation. Liver MAC2 expression by immunohistochemistry (Figure 4E) confirmed CDAHFD-LIE mouse livers to have reduced macrophage infiltration compared to the CDAHFD-scr controls, both in male and female mice. Picrosirius red staining, indicative of fibrosis, demonstrated that CDAHFD-scr male mice had substantial pericellular fibrosis with a reduction in the CDAHFD-LIE male mouse livers by quantification of the picrosirius red positive area (Figure 4, E and F). Fibrogenic gene assessment demonstrated upregulation of *Timp1* and *aSMA* genes in male CDAHFD-scr group compared to the con-scr which were downregulated in the CDAHFD-LIE group (Supplemental Figure 7, J-K). *Col1a1* transcripts followed a similar trend, although the datapoints did not achieve statistical significance (Supplemental Figure 7L).

Picrosirius red staining and fibrogenic gene expression studies showed no fibrosis in the female CDAHFD-scr or the CDAHFD-LIE mouse livers compared to the con-scr mouse livers (Figure 4, E-F, and Supplemental Figure 7, J-L). Taken together, our data demonstrates that repression of a murine LIE element on the *S100a11* promoter in a CDAHFD steatohepatitis model alleviated *S100a11* upregulation and steatohepatitis.

In vivo repression of the murine hepatic LIE abrogates high-fat, -fructose, and -cholesterol (FFC) diet-induced MASH.

In parallel, we tested if the LIE was functional in vivo in the FFC dietary model of MASH which in addition to the histological features of MASH recapitulates condition-defining cardiometabolic risks of obesity, insulin resistance, and dyslipidemia (45). In this model, insulin resistance and steatosis develop by 4 weeks of feeding (45), hence we chose a 6-week duration of FFC feeding. Mice were injected with AAV8 viral vectors prior to 6 weeks of FFC-feeding, to equilibrate Cre recombinase protein and respective sgRNAs abundance within the transduced hepatocytes, as depicted (Figure 5A). Liver/body weight ratio across the groups did not show a statistically significant difference (Supplemental Figure 8A). The ALT level was higher following 6-weeks of FFC-diet feeding in the mice injected with the scrambled construct (FFC-scr) compared to the chow fed mice (CD-scr) (Figure 5B). We noted reduction of ALT in the FFC-LIE group compared to the FFC-scr group (Figure 5B). The *iCre* expression was comparable across all virally transduced liver samples (Supplemental Figure 8B). Consistent with previous observations, the FFC-scr mice had upregulation of the expression of *S100a11* transcripts compared to CD-scr mice (Figure 5C). The FFC-LIE had attenuation of *S100a11* transcripts compared to the FFC-scr controls (Figure 5C). Assessment of *S100a10, S100a13, BiP, Atf2,* and *Ager* demonstrated no non-

specific effect of the AAV8-LIE within the FFC-LIE mouse livers (Supplemental Figure 8, C-G). Histological assessment of the liver sections demonstrated that 6 weeks of FFC caused extensive steatosis, with notable inflammatory foci, compared to the CD-scr controls (Figure 5D). FFC-scr mouse liver sections showed increased steatosis compared to the CD-scr mice, while AAV8-LIE injected FFC-fed mice showed a visual redistribution from macrovesicular to mixed macrovesicular and microvesicular steatosis compared to the FFC-scr mice. BODIPY staining of the liver sections and quantification demonstrated a range of steatosis in the FFC-fed mice, however the levels were comparable between the FFC-scr and FFC-LIE mouse livers (Supplemental Figure 8, H-I). Assessment of the inflammatory foci demonstrated reduction within the FFC-LIE mice groups compared to FFC-scr controls (Figure 5D and Supplemental Figure 8J). Assessment of macrophage accumulation by immunohistochemistry and qPCR also confirmed an increase in inflammatory macrophage abundance in FFC-scr and reduction in FFC-LIE mice (Figure 5, D and E). Picrosirius red staining demonstrated an increase in pericellular collagen fibers in FFC-scr compared to the CD-scr groups, with a reduction in fibrosis in the FFC-LIE mouse livers (Figure 5, D and F). qPCR analysis of mouse livers showed upregulation of *Timp1*, *aSMA* and *Mmp12* transcripts in FFC-scr mice compared to the CD-scr mice and downregulation in the FFC-LIE group to levels similar to CD-scr mice (Supplemental Figure 8, K-M). Taken together, our data demonstrate that repression of the murine LIE element on the *S100a11* genomic region in FFC-diet fed *dCas9-KRAB* mice led to a definitive reduction in liver injury, inflammation, and fibrosis following the repression of an *S100a11* transcriptional program.

Fibrosis can be attenuated due to etiological reversal or due to direct effects on hepatic stellate cells. While we noted a reduction in injury and inflammation in both MASH models treated with LIE sgRNA, consistent with etiological reversal, we also asked if S100A11 may have direct

effects on hepatic stellate cells via its cognate receptor, the receptor for advanced glycation end-products (RAGE). We treated LX-2 cells (human hepatic stellate cell line) with recombinant human S100A11 protein and measured the expression of fibrogenic genes. S100A11 treatment upregulated *aSMA, TIMP1, COL1A1* transcripts compared to respective controls (Supplemental Figure 9, A-C), suggesting a potential hepatocyte to stellate cell signaling axis mediated by S100A11 in MASH. In our recent work (44), we have reported the interaction between S100A11 and RAGE in macrophages to be vital in the proinflammatory response in MASH livers. Thus, taken together, we demonstrate that S100A11, enriched on EVs and derived from lipotoxic hepatocyte under the control of a LIE element, can have pleotropic outcomes through signaling responses in macrophages and hepatic stellate cells.

DISCUSSION

MASH is a hepatic manifestation of the metabolic syndrome and demonstrates hepatic lipotoxicity induced sterile inflammation. DAMPs or alarmins secreted from lipotoxic hepatocytes regulate proinflammatory immune cell accumulation and activation in the liver. In this study we report: (a) lipotoxic hepatocytes secrete S100A11 on extracellular vesicles; (b) palmitate-induced hepatic lipotoxicity upregulates S100A11 via IRE1A-XBP1s signaling; (c) palmitate-induced lipotoxic ER stress epigenetically activates a distal regulatory element in the S100A11 genomic locus, which we have termed a LIE domain, demonstrated by enhanced H3K27ac marks; (d) dCas9-KRAB-mediated repression of the LIE lowers lipotoxicity-induced *S100a11* upregulation and associated inflammatory foci within the hepatic parenchyma of murine steatohepatitic livers; (e) there is an increase in S100A11-expressing hepatocyte-derived EVs in human MASH plasma samples; and (f) there is increased occupancy of p300 and XBP1s with H3K27ac on the LIE domain in human MASH liver samples along with an increase in *S100A11* transcript expression. These in vitro and in vivo observations present an integral crosstalk between lipotoxic ER stress and epigenetic regulation through a LIE domain which regulates the expression of S100A11.

Lipotoxicity is an essential step in hepatocellular injury in MASH, leading to both sublethal and lethal responses (46). Sublethal lipotoxic responses include organelle stress, such as ER stress, and the release of extracellular vesicles (EVs). Studies have shown that EVs are qualitatively and quantitatively altered in MASH (10). Using an unbiased proteomics approach, this study identified the DAMP, S100A11, to be enriched on lipotoxic EVs, in keeping with previous findings (11). Analysis of donor lipotoxic hepatocytes, from which the EVs originated, demonstrated lipotoxicity induced transcriptional upregulation of *S100A11*. The role of ER stress in this transcriptional

program was investigated due to our earlier observations that lipotoxicity activates the ER stress response and that IRE1A activation drives the release of EVs from hepatocytes (10, 19).

Palmitate can activate all three UPR sensors; therefore, we employed specific pharmacological inhibitors for each of the three sensors followed by confirmatory experiments in IRE1A-KO-IMH cells to demonstrate that deficiency of IRE1A attenuated the upregulation of *S100A11* transcripts in palmitate-treated hepatocytes. Mass spectrometric assessment of S100A11 abundance on EVs corresponded with the mRNA abundance. As mass spectrometry is not inherently quantitative, we confirmed these observations using SPR, which demonstrated an increase in S100A11-expressing EVs derived from WT-IMH cells and lack thereof in IRE1A-KO-IMH cells. Taken together, we identified hepatic S100A11 as a readout of lipotoxic ER stress, transcriptionally upregulated by IRE1A signaling and released on EVs.

IRE1A activation leads to generation of spliced XBP1, the transcriptionally active form an evolutionarily conserved basic region/leucine zipper family transcription factor (47). We identified an XBP1s consensus motif on the promoter of *S100A11* which demonstrated XBP1s occupancy and activity, yet it was not essential for the expression of *S100A11*, suggesting additional regulatory elements such as enhancers. It has been reported that XBP1s interaction with p300 enhances its transcriptional activity (32, 33), potentially via enhancers and superenhancers (48). Thus, we investigated a potential enhancer domain in the context of palmitate-stimulated XBP1s activation. Initial analysis of publicly available H3K27ac ChIP-Seq datasets identified an H3K27ac genomic region, marking a potentially active enhancer (37), upstream to the *S100A11* promoter. While H3K27ac was detected under the variable conditions of the published data sets, we empirically tested the relevance of this genomic region under lipotoxic conditions. In subsequent ChIP-qPCR studies we found this putative genomic region, which we named LIE, to be acetylated basally and

demonstrate increased acetylation following palmitate stimulation. Furthermore, we confirmed the co-occupancy of XBP1s and p300 proteins on the LIE region. Using a dCas9-KRAB-mediated CRISPRi approach (41) and LIE-specific single guide RNAs, we demonstrated that repression of the LIE attenuated palmitate-induced H3K27ac active marks on the LIE domain and *S100A11* transcripts. Based on our data, we propose that metabolic stress like lipotoxic ER stress causes increased recruitment of XBP1s and p300 to the LIE domain leading to hyperactivity of the putative enhancer (LIE) and upregulation of S100A11. These data also suggest that lipotoxic ER stress hijacks an already active enhancer to mediate transcriptional upregulation of S100A11 in hepatocytes.

Enhancer elements function as a unique epigenetic platform for highly organized tissue-specific transcription. We aimed to repress the LIE region and assess hepatic *S100a11* levels in two well-established murine MASH models (42, 43) (45). Repression of the LIE domain led to attenuation of hepatic *S100a11* mRNA levels in AAV8-sg-LIE injected mice in comparison to the AAV8-sg-scr injected control mice, which was associated with a reduction in liver injury, inflammation, and fibrosis. There was a difference in the pattern of steatosis in FFC-LIE compared FFC-scr mouse livers, with greater microvesicular steatosis, suggesting a role for S100A11 in hepatic steatosis. Indeed, S100A11 is known to promote lipogenesis via FOXO-1 (27), which may explain the observed differences in the pattern of steatosis. There was a reduction in inflammatory foci and macrophage accumulation in CDAHFD-LIE and FFC-LIE groups compared to the controls. Recently, we reported the role of RAGE-expressing macrophages in mediating liver proinflammatory macrophage accumulation (44). Our previous study postulated but did not identify a potential endogenous ligand for RAGE expressing macrophages. In this study we have

identified that S100A11 is upregulated in MASH, and its inhibition attenuates macrophage accumulation, suggesting its role as an endogenous RAGE ligand in MASH.

In parallel we observed a reduction in fibrosis and the expression of fibrogenic genes following LIE repression in male mice on MASH-inducing CDAHFD and FFC diets. Female CDAHFD-fed mice did not develop appreciable fibrosis consistent with the reported resistance of female mice to CDAHFD-induced fibrosis (49). A reduction in injury and inflammation can lead to a reduction in liver fibrosis; however, we cannot exclude a direct effect of hepatocyte-derived S100A11-enriched EVs on hepatic stellate cells as our studies with recombinant S100A11 protein and LX-2 cells demonstrated upregulation of fibrogenic genes. Thus, we believe that hepatocyte-derived S100A11 may have pleiotropic effects in the liver. The focus of the current study has been on defining the LIE domain in hepatocytes and its regulation of *S100A11* under lipotoxic conditions. Further studies with hepatic stellate cells are beyond the scope of the current work and could be examined in the future. Taken together, our study highlights a functional enhancer element, termed LIE, within the S100A11 regulatory framework that plays a key role in liver injury and inflammation associated with MASH progression.

To extend these observations to human MASH we demonstrated that circulating hepatocyte-derived EVs are increased in MASH plasma compared to controls, consistent with the findings of several other groups (25, 50). In this study, we further demonstrate that S100A11 is enriched on each hepatocyte-derived EV in MASH plasma samples. Correspondingly, *S100A11* transcript is upregulated and there is an increase in the occupancy of p300 and XBP1s on the LIE domain along with an increase in H3K27ac. Thus, our findings confirm the relevance of lipotoxic ER stress-induced upregulation of S100A11 in MASH.

In conclusion, our study established a fundamental association between lipotoxic ER stress and epigenetics within the transcriptional program of *S100A11* in a lipotoxic hepatic milieu. We have defined an H3K27ac marked active chromatin region upstream to the transcription start site of the *S100A11* gene as a LIE domain in lipotoxicity cell culture models, murine MASH, and human MASH. Targeted repression of this region employing dCas9-KRAB methodology attenuated *S100A11* transcript levels and MASH. We present *S100A11* as a potentially druggable target to curb steatohepatitis and thereby reduce the severity and rate of MASH progression.

METHODS

Sex as a biological variable. We employed two diet-induced murine MASH models for the study. Both male and female *dCas9-KRAB* mice were used for the CDAHFD feeding because the disease penetrance is similar in both sexes. Only male *dCas9-KRAB* mice were used for the FFC-diet feeding as female mice are resistant to FFC-diet induced obesity and MASH (45).

Mouse studies. Animal use was approved by the Institutional Care and Animal Use Committee of the Mayo Clinic and conducted in accordance with the public health policy on the humane use and care of laboratory animals. *dCas9-KRAB* expressing C57BL/6J background mice (Jax, #033066) were used for all experiments, were procured as a kind gift from Dr. Vijay Shah and are available from Jackson laboratory. Mice were housed in a 12-hour dark/light cycle. Mice were fed rodent chow diet (CD) or at 10-12 weeks of age switched to steatohepatitis-inducing diets. One group was fed with a choline-deficient, L-amino acid-defined, high-fat diet (CDAHFD) for 3 weeks to induce steatohepatitis (42, 43) along with the respective control diet to the control group. In our second model, male mice were fed with a high fat, fructose, and cholesterol (FFC) diet for 6 weeks to recapitulate human MASH (45). This diet has been previously described and characterized by us and others as having high fidelity to human MASH (10, 44, 45). For adeno-associated virus injections, $1x10^{12}$ viral copies of AAV8-*TBG-iCre-U6-sgRNA1-H1-sgRNA2* (Vector Builder) were suspended in a total volume of 100 µl saline and injected into the tail vein. AAV8-LIE included LIE-specific sgRNA3 and sgRNA6 sequences, while AAV8-scr included two commercially generated scrambled sgRNAs. Sequence of each sgRNA is available in Supplementary Table 1. On completion of the study, mice were sacrificed, tissues were harvested, and platelet poor plasma samples were analyzed for biochemistry parameters using a commercial veterinary chemistry analyzer (VetScan 2; Abaxis). Viral transduction was verified by PCR and

confirmed by sequencing using the following steps. Briefly, a small piece of the mouse liver was processed using the Zymo DNA extraction kit to isolate the whole liver genomic DNA. PCR primers were used to amplify specific amplicons from each vector backbone, and the PCR amplicon was gel extracted and sequenced (Azenta). The DNA of the sgRNA for mouse LIE regions were checked for sequence similarity. AAV8-scr was also sequenced but only AAV8-LIE sequencing chromatogram is shown (Supplemental Figure 7C).

Cell culture-based studies. Huh7 cells were obtained from Dr. Sanjeev Gupta (and are available from JCRB #JCRB0403) and maintained in DMEM supplemented with 10% FBS and 1% penicillin-streptomycin antibiotics. WT (homozygous IRE-floxed)- and IRE-KO-IMH cells were obtained from Dr. Randal Kaufman's lab and have been previously described (11, 19, 20). IMHs were maintained in the same media as above with an additional 1% non-essential amino acids (NEAA). For palmitate-mediated lipotoxicity experiments, a stock of 80 mM palmitic acid (Millipore Sigma, P0500) was prepared in molecular grade isopropanol and further diluted to a final concentration of 600 μM (for Huh7 cells), 400 μM (for IMH cells), and 400 μM (for PMH cells) in 10% FBS-containing media and supplemented with 1% BSA. Inhibitor studies were performed with concurrent treatment with palmitic acid and inhibitor. For EV based experiments, EV-free FBS was used in all treatment media preparations. For transfection-based experiments, overnight seeded 70-80 % confluent Huh7 cell monolayers were treated with respective plasmids complexed with GenJet™ reagent, following manufacturer's protocol and experiments were conducted within 24-48 hours. *dCas9-KRAB*-expressing Huh7 cells and IMH cells were prepared using the lentiviral plasmid (Addgene, 89567). sgRNA (Integrated DNA Technologies) were transfected using Lipofectamine RNAimax (Invitrogen). sgRNA sequences used for human-LIE repression for in vitro studies are listed in Supplementary Table 1. Acetyl Co-A levels were

549 measured employing a commercially available assay, as per the manufacturer's protocol (Sigma,
550 MAK039). Human stellate cell line, LX-2 (a kind gift of Dr. Scott Friedman), were maintained in
551 10% FBS containing DMEM. LX-2 cells were treated with recombinant human S100A11 protein
552 (SinoBiological, 11140-HNAE) as follows: 5 x 10^5 LX-2 cells/well were seeded in a 6-well plate
553 and after overnight adherence, cells were serum starved for 30 mins in 1% FFA-BSA containing
554 DMEM. Cells were treated with 100 ng/mL of rS100A11 for 4 h (44). Cells were lysed in TRIzol
555 for RNA isolation and gene expression analysis as described below.
556 **Primary mouse hepatocytes**. PMH were isolated via portal vein perfusion using a two-step
557 collagenase based protocol (51). The dissociated cells were further passed through a 70 μm filter
558 and gently centrifuged at 50 x g for 2 minutes. The pelleted hepatocytes were purified using
559 buffered Percoll in serum free DMEM at 200 x g for 10 minutes. Cell viability was assessed and
560 PMHs were plated on collagen coated dishes for experiments.
561 **Human samples.** Available biobanked human liver specimens and plasma samples, collected from
562 MASH patients and obese normal patients as previously published (52, 53) and MASH and normal
563 control samples from a Mayo Clinic Biobank were used following approval by the Mayo Clinic
564 IRB and written informed consent for medical research. The diagnosis of MASH and histologically
565 normal liver was established by expert pathologist review. In the MASH samples fibrosis stage
566 ranged from 1 to 3.
567 **EV isolation and proteomics.** EVs were collected from the cell culture supernatants using
568 Differential Ultracentrifugation (UTC) (10, 11). Cell supernatants were collected and centrifuged
569 at 2000 × g for 10 minutes to remove cellular debris. To isolate large EVs, the supernatant was
570 centrifuged at 10,000 × g for 10 minutes, termed the 10 pellet, and the resultant supernatant was
571 then transferred to a UTC compatible, open-top thick-wall polypropylene tube (Beckman Coulter)

and centrifuged at 100,000 × g for 90 minutes to pellet small EVs, termed the 100K EVs. The pellets were washed in PBS, following a 100,000 × g for 2 h and resuspended in PBS, until further use. 100K EVs were used for EV proteomics and immunogold labelling. EV proteomics were performed at the Mayo Clinic Proteomics Core Laboratory, as described previously (11). EVs were characterized by electron microscopy (EM) and immunogold staining using S100A11 antibodies with gold-protein A particles (10). EVs were prepared as whole mounts, labeled with immunogold, and negatively stained to visualize only the surface proteins. Objects were observed with JEOL 1400 electron microscope (10). For the S100A11 ELISA, both 10K and 100K EVs were isolated from Huh7 cell culture supernatants, and S100A11 levels were measured according to the manufacturer's protocol (Invitrogen, EH397RB).

SPR assay. Biosensing instruments SPR (Bi-2500) was used for analysis. Plasma samples from patients with MASH and healthy controls were processed by ultracentrifugation at 110,000 × g for 2 h to isolate EVs and isolated EVs were analyzed using NTA instrument (Malvern, NS300) to measure EV concentration (19). Subsequently MASH and control EVs were resuspended in 1× PBS buffer at the same concentration. Prior to analysis, gold-coated SPR chip was functionalized with 11-Mercaptoundecanoic acid (MUA, Sigma-Aldrich) in a manner described previously (54) to immobilize anti-ASGR2. EVs at a concentration of 2×10^9 particles/mL in 1x PBS were infused into the SPR instrument at 10 µL/min flow rate for 10 minutes. Subsequently, the SPR chip was flushed with washing buffer (1× PBS) for 5 min to remove excess unbound EVs. SPR signals associated with EV capture represented the difference of the signal before the introduction of EVs and after washing buffer. Subsequently, anti-S100A11 (10 µg/mL in 1× PBS buffer) was injected into SPR instrument for 5 min with a flow rate of 20 µL/min. The washing buffer was introduced for 5 min to remove excess Abs. The SPR signal for S100A11 expression was taken as the

595 difference of SPR signals before Ab and after washing. Subsequently, CYP2E1 and rabbit IgG
596 antibodies were sequentially assayed. The binding results for each sample were obtained from
597 three different (parallel) channels of the SPR instrument.

598 **Gene promoter assessments.** Publicly available hepatocyte/liver H3K27ac ChIP-Seq GEO
599 datasets (BigWig files) were read on the Integrative Genomics Viewer (IGV) platform and assessed
600 for H3K27ac marks on the promoter of *S100A11*. Publicly available hepatocyte/liver ATAC files
601 were also used to compare plausible TF-binding regions on the enhancer domain to make specific
602 primers which would enable a distinction between H3K27ac based activation mark and
603 XBP1s/p300 binding. XBP1s consensus (31) localization was accounted during ChIP-qPCR
604 primer preparation to enhance the possibility of greater reads from the ChIP eluates. For promoter
605 activity, 800 base pairs of the human *S100A11* promoter upstream to the TSS was cloned into
606 pGL4.22 plasmid (Promega, E6771) following conventional restriction digestion and ligation
607 method. The XBP1s site was further mutated by substitution of CCACG to AAGAT (primer
608 sequence for hS100A11 prom-M5 in Supplementary Table 2) using Q5 Site-Directed Mutagenesis
609 Kit (NEB, E0554S). The clones were sequenced to confirm cloning. A total of 1 μg of *S100A11*
610 promoter-pGL4.22 construct (0.75 ng) was then co-transfected with TK-*Renilla* (0.25 ng) into
611 Huh7 cells using GenJet™ reagent, in a 24-well plate. The cells were lysed after treatment using
612 the Dual-Glo reagent (Promega) and relative luminescence units for both Firefly and Renilla were
613 recorded.

614 **ChIP assay.** To assess enrichment of XBP1s, p300, and H3K27ac mark on genomic regions, ChIP
615 assay was performed using ChIP-IT® Express kit (Active-Motif, 53008). Briefly, after respective
616 treatments, cultured cells were formalin fixed and weakly lysed to release intact nuclei. For human
617 liver ChIP, intact nuclei were released from frozen tissue by mincing approximately 100mg of

frozen tissue in 700 µL 1% formaldehyde followed by addition of 10x glycine solution to stop the reaction. This was pelleted and washed with PBS. The pellet was subsequently dounced and incubated in 500 µL ice-cold Lysis Buffer for 30 minutes after which nuclei were pelleted. Isolated nuclear pellets were lysed in the shearing buffer followed by optimized sonication-based chromatin fragmentation (25 Hz, cycle setting of 20 s on/off, five times with a break of 1 min between each cycle). An aliquot of the chromatin was cleared for total DNA content quantification and an equal amount of chromatin was further processed for the ChIP assay. Appropriate isotype controls were also included alongside specific antibodies for ChIP pulldown. Elution of the antibody-bound specific chromatin after required number of washes was performed following the manufacturers protocol. The eluate was then assessed for protein-interacting genomic regions via qPCR (primer sequences available in Supplementary Table 2) and a fold change between treatment groups for a specific antibody was calculated. Respective antibody concentrations and their catalogue numbers are listed in Supplementary Table 3.

qPCR analyses. For in vitro experiments, cells were lysed in TRIzol, and total RNA was extracted using a commercially available kit (Zymo) following manufacturers protocol. For mice/human liver tissue samples, 5-10 mg of tissues were homogenized in TRIzol and proceeded with RNA extraction using a kit (Zymo). 1 µg of total RNA was further processed to prepare cDNA using iScript cDNA preparation kit, following the manual. Diluted cDNA samples were assessed via quantitative PCR and relative fold change was calculated using the ΔΔCT method (55). 1 µL of diluted cDNA was used as a template for reverse transcription PCR based electrophoretic XBP1 splicing assessment (56). Three or more biological replicates were performed for each qPCR assay. 18S was used as loading control unless otherwise stated. Primer sequences are listed in Supplementary Table 2.

Western Blotting. Cell or tissue lysates were prepared in RIPA buffer supplemented with a protease inhibitor cocktail. Total protein was quantified using BCA assay (Thermo). 20-30 µg of protein was resolved onto a 4-20% gradient polyacrylamide SDS gel (Biorad) and immunoblotted onto a 0.22 µm PVDF membrane using Tris-Glycine transfer buffer. Non-specific proteins were blocked with 5% nonfat dairy milk in TBS-T for 1 h at room temperature and incubated with primary antibodies diluted in 5% BSA in TBS-T overnight at 4ºC. Next day, membranes were washed, treated with respective secondary antibodies diluted in 5% nonfat dairy milk in TBS-T at room temperature. Following another set of TBST washes, signals were visualized using ECL based chemiluminescence and developed using film. Western blot densitometry was performed using ImageJ. Antibodies used for the study are listed in Supplementary Table 3.

Histological studies. H&E staining was performed by the Mayo Clinic Histology Core, Arizona (10). For immunohistochemistry (IHC), formalin-fixed paraffin embedded (FFPE) tissue sections were stained with an antibody for MAC2 (Supplementary Table 3) using the ABC Immunostaining kit (Vector Laboratories) protocol. Fibrosis was assessed by Picrosirius red staining and quantified by the polarized light microscope method as described previously (44). BODIPY staining of mouse liver sections were performed as described previously (57).

Statistical analysis. All experimental datasets represent mean ± SEM of datapoints obtained from three or more biological replicates. For two experimental groups, two-tailed Student's t-test was used for statistical analyses in GraphPad Prism 9. Multiple treatment groups were analyzed using one-way or two-way ANOVA test, with Bonferroni or Šídák corrections. A *P* value less than 0.05 was considered statistically significant. Outliers were identified using Grubbs' test and removed from analysis.

Study approval. Mouse procedures were reviewed and approved by the Mayo IACUC (Rochester, Minnesota). Biobanked human liver tissue samples and plasma samples were obtained following Mayo Clinic IRB (Rochester, Minnesota) approval and written informed consent from patients.

Data availability. A Source Data file containing all reported data values is included in the supplemental materials. Unedited gel images are also included in the supplemental materials. Publicly available H3K27ac ChIP-seq datasets were accessed from the GEO database for liver cell line (GSM2360939_Huh7, GSM5911467_HepG2, and GSE168186_Hu1545), mouse liver (GSM5173253_A761, GSM5173254_A787, GSM4455320_Y.8.1, and GSM5404619_DKO_rep2), and human liver (GSM1112809_Adult_Liver4) samples.

AUTHOR CONTRIBUTONS

H.M. conceived the project. H.M, P.V.D, F.H.H, designed the experiments. P.V.D, H.L.E, A.S.M, G.P, Y.N, Y.Y, D.D, and T.N. conducted the experiments and interpreted the results. D.C executed the SPR analysis supervised by A.R and H.M. J.T helped with tail vein injections. H.M. provided all the reagents. P.V.D., H.L.E., and H.M. wrote the manuscript. All authors contributed to manuscript editing and provided a critical review and approval of the manuscript.

678 **ACKNOWLEDGEMENTS**

679 The authors are grateful to Ms. Courtney Hoover for superb administrative assistance. Authors
680 acknowledge Dr. Michael Charlton, Dr. Anuradha Krishnan, Dr. Konstantinos N. Lazaridis, Dr.
681 Maria Eugenia Guicciardi, Dr. Lisa Boardman, Mrs. Annika Tate, and Mrs. Donna D. Devine for
682 helping with access to patient plasma and liver samples. The WT-IMH and IRE1A-KO-IMH were
683 kindly provided by Dr. Randal Kaufman. This work is supported by NIH grant DK111378 (to
684 H.M.), DK134661 (A.R.) the Mayo Foundation (to H.M.), the Optical Microscopy Core and the
685 Clinical Core of the Mayo Clinic Center for Cell Signaling in Gastroenterology (P30DK084567),
686 and the Histology Core of the Mayo Clinic. P.V.D. gratefully acknowledges the American Liver
687 Foundation Postdoctoral Research Fellowship Award 2024. This work is the result in part of NIH
688 funding and is subject to the NIH Public Access Policy. Through acceptance of this federal funding,
689 the NIH has been given a right to make the work publicly available in PubMed Central.

REFERENCES:

1. Yang D, Han Z, and Oppenheim JJ. Alarmins and immunity. *Immunol Rev.* 2017;280(1):41-56.
2. Wang H, Mehal W, Nagy LE, and Rotman Y. Immunological mechanisms and therapeutic targets of fatty liver diseases. *Cellular & Molecular Immunology.* 2021;18(1):73-91.
3. Bertheloot D, and Latz E. HMGB1, IL-1α, IL-33 and S100 proteins: dual-function alarmins. *Cellular & Molecular Immunology.* 2017;14(1):43-64.
4. Wang X, Wang Y, Antony V, Sun H, and Liang G. Metabolism-Associated Molecular Patterns (MAMPs). *Trends Endocrinol Metab.* 2020;31(10):712-24.
5. Han J, and Kaufman RJ. The role of ER stress in lipid metabolism and lipotoxicity. *J Lipid Res.* 2016;57(8):1329-38.
6. Cazanave SC, and Gores GJ. Mechanisms and clinical implications of hepatocyte lipoapoptosis. *Clin Lipidol.* 2010;5(1):71-85.
7. Hirsova P, Ibrahim SH, Krishnan A, Verma VK, Bronk SF, Werneburg NW, et al. Lipid-Induced Signaling Causes Release of Inflammatory Extracellular Vesicles From Hepatocytes. *Gastroenterology.* 2016;150(4):956-67.
8. Rada P, González-Rodríguez Á, García-Monzón C, and Valverde ÁM. Understanding lipotoxicity in NAFLD pathogenesis: is CD36 a key driver? *Cell Death & Disease.* 2020;11(9):802.
9. Zaborowski MP, Balaj L, Breakefield XO, and Lai CP. Extracellular Vesicles: Composition, Biological Relevance, and Methods of Study. *Bioscience.* 2015;65(8):783-97.
10. Dasgupta D, Nakao Y, Mauer AS, Thompson JM, Sehrawat TS, Liao C-Y, et al. IRE1A Stimulates Hepatocyte-Derived Extracellular Vesicles That Promote Inflammation in Mice With Steatohepatitis. *Gastroenterology.* 2020;159(4):1487-503.e17.
11. Nakao Y, Fukushima M, Mauer AS, Liao CY, Ferris A, Dasgupta D, et al. A Comparative Proteomic Analysis of Extracellular Vesicles Associated With Lipotoxicity. *Front Cell Dev Biol.* 2021;9:735001.
12. Sveinbjornsson G, Ulfarsson MO, Thorolfsdottir RB, Jonsson BA, Einarsson E, Gunnlaugsson G, et al. Multiomics study of nonalcoholic fatty liver disease. *Nat Genet.* 2022;54(11):1652-63.
13. Hardy T, and Mann DA. Epigenetics in liver disease: from biology to therapeutics. *Gut.* 2016;65(11):1895-905.
14. Gallego-Durán R, and Romero-Gómez M. Epigenetic mechanisms in non-alcoholic fatty liver disease: An emerging field. *World J Hepatol.* 2015;7(24):2497-502.
15. Wang S, Zha L, Cui X, Yeh YT, Liu R, Jing J, et al. Epigenetic Regulation of Hepatic Lipid Metabolism by DNA Methylation. *Adv Sci (Weinh).* 2023;10(20):e2206068.
16. Sehgal R, Perfilyev A, Männistö V, Ågren J, Nilsson E, Käkelä P, et al. Liver saturated fat content associates with hepatic DNA methylation in obese individuals. *Clinical Epigenetics.* 2023;15(1):21.
17. Mann DA. Epigenetics in liver disease. *Hepatology.* 2014;60(4):1418-25.
18. Zovkic IB, Guzman-Karlsson MC, and Sweatt JD. Epigenetic regulation of memory formation and maintenance. *Learn Mem.* 2013;20(2):61-74.
19. Kakazu E, Mauer AS, Yin M, and Malhi H. Hepatocytes release ceramide-enriched pro-inflammatory extracellular vesicles in an IRE1α-dependent manner. *J Lipid Res.* 2016;57(2):233-45.
20. Zhang K, Wang S, Malhotra J, Hassler JR, Back SH, Wang G, et al. The unfolded protein response transducer IRE1alpha prevents ER stress-induced hepatic steatosis. *EMBO J.* 2011;30(7):1357-75.
21. Roh JS, and Sohn DH. Damage-Associated Molecular Patterns in Inflammatory Diseases. *Immune Netw.* 2018;18(4):e27.
22. Gonzalez LL, Garrie K, and Turner MD. Role of S100 proteins in health and disease. *Biochimica et Biophysica Acta (BBA) - Molecular Cell Research.* 2020;1867(6):118677.

23. Buzás EI, Tóth E, Sódar BW, and Szabó-Taylor K. Molecular interactions at the surface of extracellular vesicles. *Semin Immunopathol.* 2018;40(5):453-64.
24. Nakao Y, Amrollahi P, Parthasarathy G, Mauer AS, Sehrawat TS, Vanderboom P, et al. Circulating extracellular vesicles are a biomarker for NAFLD resolution and response to weight loss surgery. *Nanomedicine.* 2021;36:102430.
25. Povero D, Yamashita H, Ren W, Subramanian MG, Myers RP, Eguchi A, et al. Characterization and Proteome of Circulating Extracellular Vesicles as Potential Biomarkers for NASH. *Hepatol Commun.* 2020;4(9):1263-78.
26. Sobolewski C, Abegg D, Berthou F, Dolicka D, Calo N, Sempoux C, et al. S100A11/ANXA2 belongs to a tumour suppressor/oncogene network deregulated early with steatosis and involved in inflammation and hepatocellular carcinoma development. *Gut.* 2020;69(10):1841-54.
27. Zhang L, Zhang Z, Li C, Zhu T, Gao J, Zhou H, et al. S100A11 Promotes Liver Steatosis via FOXO1-Mediated Autophagy and Lipogenesis. *Cell Mol Gastroenterol Hepatol.* 2021;11(3):697-724.
28. Cnop M, Foufelle F, and Velloso LA. Endoplasmic reticulum stress, obesity and diabetes. *Trends Mol Med.* 2012;18(1):59-68.
29. Parthasarathy G, Hirsova P, Kostallari E, Sidhu GS, Ibrahim SH, and Malhi H. Extracellular Vesicles in Hepatobiliary Health and Disease. *Compr Physiol.* 2023;13(3):4631-58.
30. Maiers JL, and Malhi H. Endoplasmic Reticulum Stress in Metabolic Liver Diseases and Hepatic Fibrosis. *Semin Liver Dis.* 2019;39(2):235-48.
31. Acosta-Alvear D, Zhou Y, Blais A, Tsikitis M, Lents NH, Arias C, et al. XBP1 controls diverse cell type- and condition-specific transcriptional regulatory networks. *Mol Cell.* 2007;27(1):53-66.
32. Wang F-M, Chen Y-J, and Ouyang H-J. Regulation of unfolded protein response modulator XBP1s by acetylation and deacetylation. *Biochemical Journal.* 2010;433(1):245-52.
33. Lew QJ, Chu KL, Lee J, Koh PL, Rajasegaran V, Teo JY, et al. PCAF interacts with XBP-1S and mediates XBP-1S-dependent transcription. *Nucleic Acids Res.* 2011;39(2):429-39.
34. Ibrahim Z, Wang T, Destaing O, Salvi N, Hoghoughi N, Chabert C, et al. Structural insights into p300 regulation and acetylation-dependent genome organisation. *Nat Commun.* 2022;13(1):7759.
35. Zeng L, Liu YP, Sha H, Chen H, Qi L, and Smith JA. XBP-1 couples endoplasmic reticulum stress to augmented IFN-beta induction via a cis-acting enhancer in macrophages. *J Immunol.* 2010;185(4):2324-30.
36. Zhang Y, Xue Y, Shi J, Ahn J, Mi W, Ali M, et al. The ZZ domain of p300 mediates specificity of the adjacent HAT domain for histone H3. *Nature Structural & Molecular Biology.* 2018;25(9):841-9.
37. Ko JY, Oh S, and Yoo KH. Functional Enhancers As Master Regulators of Tissue-Specific Gene Regulation and Cancer Development. *Mol Cells.* 2017;40(3):169-77.
38. Pennacchio LA, Bickmore W, Dean A, Nobrega MA, and Bejerano G. Enhancers: five essential questions. *Nat Rev Genet.* 2013;14(4):288-95.
39. Gilbert LA, Larson MH, Morsut L, Liu Z, Brar GA, Torres SE, et al. CRISPR-mediated modular RNA-guided regulation of transcription in eukaryotes. *Cell.* 2013;154(2):442-51.
40. McDonnell E, Crown SB, Fox DB, Kitir B, Ilkayeva OR, Olsen CA, et al. Lipids Reprogram Metabolism to Become a Major Carbon Source for Histone Acetylation. *Cell Rep.* 2016;17(6):1463-72.
41. Gemberling MP, Siklenka K, Rodriguez E, Tonn-Eisinger KR, Barrera A, Liu F, et al. Transgenic mice for in vivo epigenome editing with CRISPR-based systems. *Nat Methods.* 2021;18(8):965-74.
42. Matsumoto M, Hada N, Sakamaki Y, Uno A, Shiga T, Tanaka C, et al. An improved mouse model that rapidly develops fibrosis in non-alcoholic steatohepatitis. *Int J Exp Pathol.* 2013;94(2):93-103.
43. Kawachi Y, Fujishima Y, Nishizawa H, Nakamura T, Akari S, Murase T, et al. Increased plasma XOR activity induced by NAFLD/NASH and its possible involvement in vascular neointimal proliferation. *JCI Insight.* 2021;6(17).

44. Parthasarathy G, Mauer AS, Golla N, Daniel PV, Kim LH, Sidhu GS, et al. Macrophage RAGE activation is proinflammatory in NASH. *JCI Insight.* 2024;9(3).
45. Krishnan A, Abdullah TS, Mounajjed T, Hartono S, McConico A, White T, et al. A longitudinal study of whole body, tissue, and cellular physiology in a mouse model of fibrosing NASH with high fidelity to the human condition. *Am J Physiol Gastrointest Liver Physiol.* 2017;312(6):G666-g80.
46. Venkatesan N, Doskey LC, and Malhi H. The Role of Endoplasmic Reticulum in Lipotoxicity during Metabolic Dysfunction-Associated Steatotic Liver Disease (MASLD) Pathogenesis. *Am J Pathol.* 2023;193(12):1887-99.
47. Yanagitani K, Kimata Y, Kadokura H, and Kohno K. Translational pausing ensures membrane targeting and cytoplasmic splicing of XBP1u mRNA. *Science.* 2011;331(6017):586-9.
48. Qiao D, Skibba M, Xu X, and Brasier AR. Genomic targets of the IRE1-XBP1s pathway in mediating metabolic adaptation in epithelial plasticity. *Nucleic Acids Res.* 2023;51(8):3650-70.
49. Lee C, Kim J, Han J, Oh D, Kim M, Jeong H, et al. Formyl peptide receptor 2 determines sex-specific differences in the progression of nonalcoholic fatty liver disease and steatohepatitis. *Nature Communications.* 2022;13(1):578.
50. Zhang W, Zhang J, Shi H, Liu F, Yu H, and Shi H. Exosome GLUT1 derived from hepatocyte identifies the risk of non-alcoholic steatohepatitis and fibrosis. *Hepatol Int.* 2023;17(5):1170-81.
51. Charni-Natan M, and Goldstein I. Protocol for Primary Mouse Hepatocyte Isolation. *STAR Protocols.* 2020;1(2):100086.
52. Charlton M, Viker K, Krishnan A, Sanderson S, Veldt B, Kaalsbeek AJ, et al. Differential expression of lumican and fatty acid binding protein-1: new insights into the histologic spectrum of nonalcoholic fatty liver disease. *Hepatology.* 2009;49(4):1375-84.
53. Guichelaar MM, Gawrieh S, Olivier M, Viker K, Krishnan A, Sanderson S, et al. Interactions of allelic variance of PNPLA3 with nongenetic factors in predicting nonalcoholic steatohepatitis and nonhepatic complications of severe obesity. *Obesity (Silver Spring).* 2013;21(9):1935-41.
54. Lee S, Verkhoturov DS, Eller MJ, Verkhoturov SV, Shaw MA, Gwon K, et al. Nanoprojectile Secondary Ion Mass Spectrometry Enables Multiplexed Analysis of Individual Hepatic Extracellular Vesicles. *ACS Nano.* 2023;17(23):23584-94.
55. Livak KJ, and Schmittgen TD. Analysis of relative gene expression data using real-time quantitative PCR and the 2(-Delta Delta C(T)) Method. *Methods.* 2001;25(4):402-8.
56. Hu J, Dang N, Menu E, De Bruyne E, Xu D, Van Camp B, et al. Activation of ATF4 mediates unwanted Mcl-1 accumulation by proteasome inhibition. *Blood.* 2012;119(3):826-37.
57. Garcia K, Alves A, Ribeiro-Rodrigues TM, Reis F, and Viana S. Analysis of Fluorescent-Stained Lipid Droplets with 3D Reconstruction for Hepatic Steatosis Assessment. *JoVE.* 2023(196):e65206.

FIGURES AND FIGURE LEGENDS:

Figure 1: S100A11 is enriched in hepatic EVs.

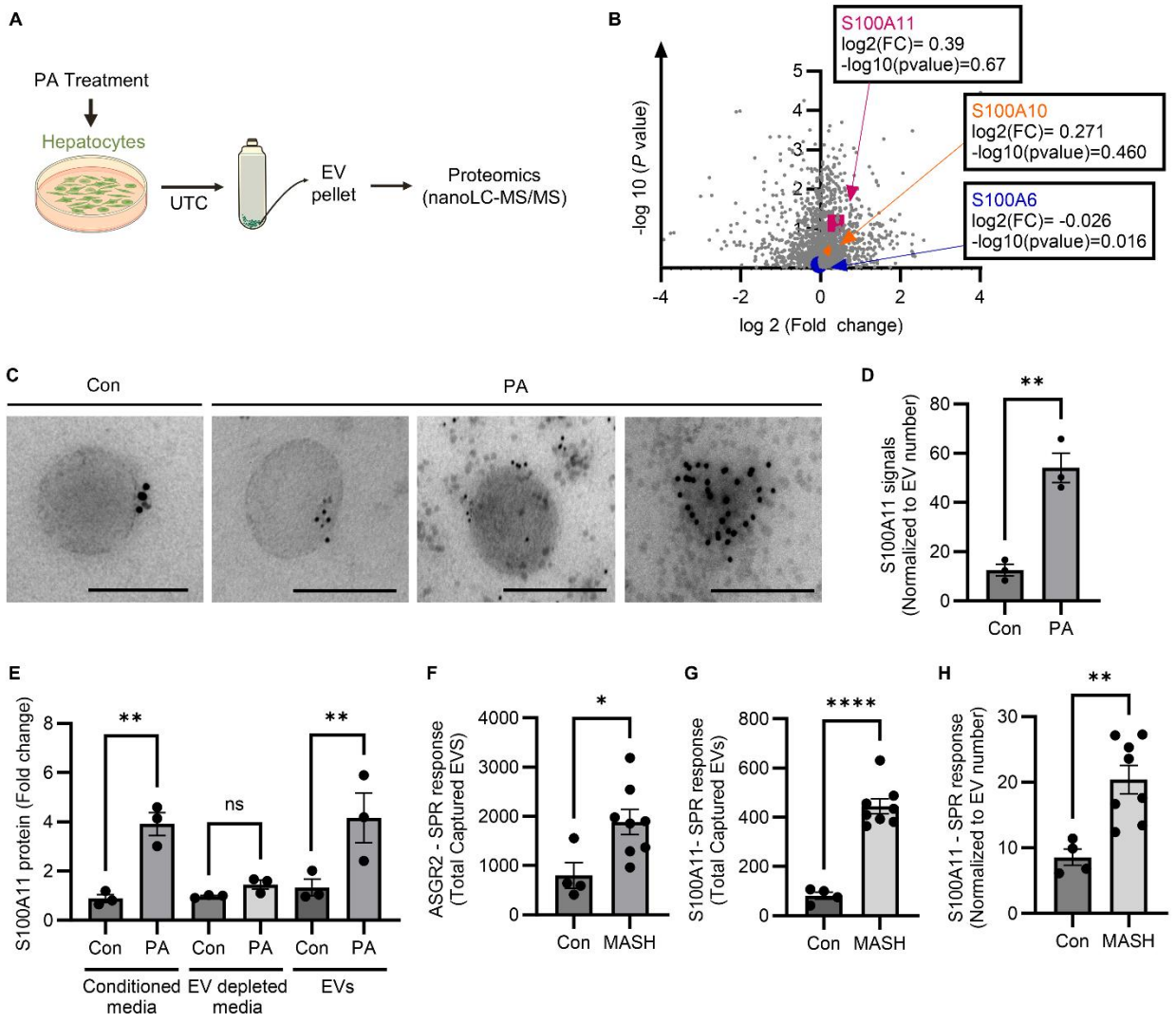

(A) Schematic representation of untargeted EV proteomics protocol following ultracentrifugation (UTC) and nano-LC-MS/MS.

(B) Volcano plot of EV proteomics performed using EVs collected from WT-IMH cells treated with 400 µM palmitate (PA) for 16 hours compared to vehicle-treated controls (n = 3 per group). S100A11 (pink square), S100A10 (orange triangle), and S100A6 (blue circle) are indicated as differentially enriched. Student's unpaired *t*-tests were used to compare two groups.

(C) Immuno-gold labelling of S100A11 (black dots) on EVs from supernatants of PMH treated with 400 μM PA or vehicle for 16 hours. Representative data is shown from n = 3 experimental replicates. Scale bar: 200 nm.

(D) SPR-based quantification of S100A11 signals in EVs isolated from PMHs treated with 400 μM PA for 16 hours compared to vehicle-treated controls (n = 3 per group). SPR response is expressed in resonance units (RU). Student's unpaired *t*-test was used to compare two groups.

(E) ELISA-based quantification of S100A11 protein in conditioned media, EV-depleted media, and EVs from Huh7 cells treated with 600 μM PA for 20 hours compared to vehicle-treated controls (n = 3 per group). One-way ANOVA with Sidak multiple comparisons test was used to compare groups.

(F) SPR based quantitative evaluation of ASGR-2-expressing hepatic EVs isolated from plasma samples from both MASH (n = 8) and control (n = 4) patients. SPR response is expressed in resonance units (RU). Student's unpaired *t*-test was used to compare two groups.

(G-H) SPR-based quantification of S100A11 abundance on ASGR-2 captured hepatic EVs from MASH (n = 8) and control (n = 4) plasma samples, expressed without (G) and with (H) EV number normalization. Student's unpaired *t*-test was used to compare two groups.

* $P < 0.05$, ** $P < 0.01$, *** $P < 0.001$, **** $P < 0.0001$.

Figure 2: IRE1A regulates lipotoxic ER stress-mediated S100A11 upregulation.

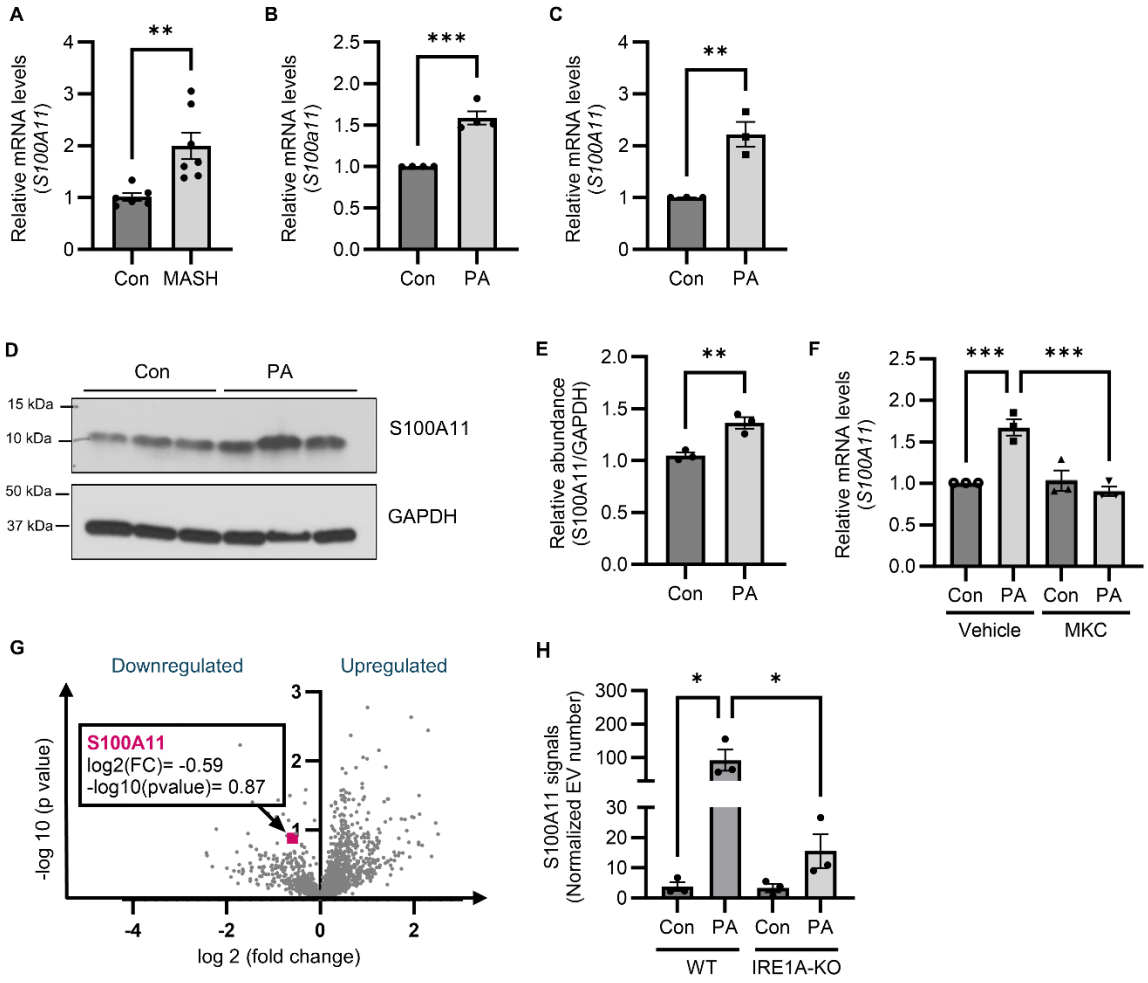

(A) Expression of *S100A11* transcript in liver from human MASH patients (n = 7) and normal controls (n = 6). Relative fold change was calculated using 18S as the loading control. Student's unpaired two-tailed *t*-test was used to compare two groups.

(B) Expression of *S100a11* transcript in PMH treated with 400 µM palmitate (PA) for 16 hours compared to vehicle-treated controls (n = 4 per group). Student's unpaired two-tailed *t*-test was used to compare two groups.

(C) Expression of *S100A11* transcript in Huh7 cells treated with 600 μM PA for 16 hours compared to vehicle-treated controls (n = 3 per group). Student's unpaired two-tailed *t*-test was used to compare two groups.

(D) WB analysis of S100A11 expression in Huh7 cells treated with 600 μM PA for 16 hours compared to vehicle treated controls (n = 3 per group).

(E) WB quantification by densitometry. Student's unpaired two-tailed *t*-test was used to compare two groups.

(F) Expression of *S100A11* transcript in Huh7 cells treated with 600 μM PA for 16 hours in the presence and absence of IRE1A inhibition with 10 μM MKC-8866 (MKC) (n = 3 per group). Two way ANOVA with Sidak multiple comparisons test was used to compare two groups with two treatments.

(G) Volcano plot of EV proteomics using EVs collected from IRE1A-KO-IMH cells treated with 400 μM PA for 20 hours compared to WT-IMH PA-treated controls (n = 3 per group). S100A11 indicated by pink square. Student's unpaired two-tailed *t*-test was used to compare two groups.

(H) SPR based quantification of S100A11 signals in EVs isolated from WT-IMH and IRE1A-KO-IMH cells treated with 400 μM PA for 20 hours compared to vehicle-treated controls (n = 3 per group). SPR response is expressed in resonance units (RU). One way ANOVA with Sidak multiple comparisons was used to compare groups.

* $P < 0.05$, ** $P < 0.01$, *** $P < 0.001$.

Figure 3: PA-induced lipotoxic ER stress epigenetically orchestrates S100A11 transcription.

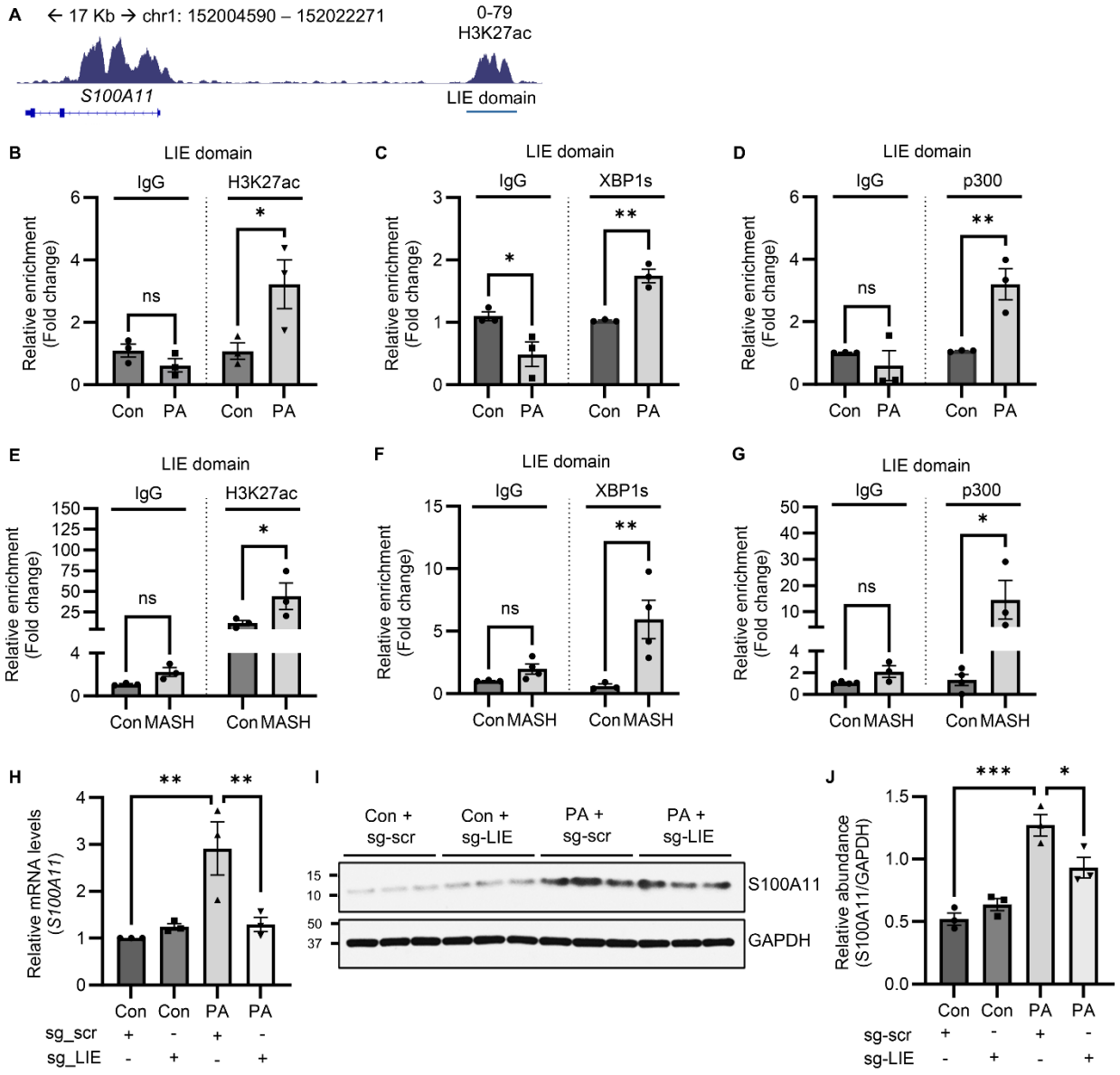

(A) Schematic representation of a H3K27ac peak (signal intensity of 0-78) on the promoter of *S100A11* gene in Huh7 genome, using Geodata set- GSM2360939_1. The co-ordinates of the enhancer region are chromosome-1: 152019738-152021345.

(B) ChIP-qPCR of H3K27ac on the LIE domain in Huh7 cells treated with 600 µM palmitate (PA) for 16 hours compared to vehicle-treated controls (n = 3 per group). Each group is normalized to

878 respective IgG control. Two way ANOVA with multiple comparisons test was used to compare
879 two groups with two conditions.
880 **(C-D)** ChIP-qPCR of **(C)** XBP1s and **(D)** p300 occupancy on the LIE domain in Huh7 cells treated
881 with 600 μM PA for 16 hours compared to vehicle-treated controls (n = 3 per group). Each group
882 is normalized to respective IgG control, which is repeated in each panel. Two way ANOVA with
883 multiple comparisons test was used to compare two groups with two conditions.
884 **(E-G)** ChIP-qPCR of **(E)** H3K27ac, **(F)** XBP1s, and **(G)** p300 occupancy on the LIE domain in
885 human MASH samples (n = 4) compared to controls (n = 4). Outliers were removed. Occupancy
886 was normalized to input then normalized to respective IgG negative control. Two way ANOVA
887 with multiple comparisons test was used to compare two groups with two conditions.
888 **(H-J)** RNA **(H)** and protein **(I-J)** expression of *S100A11* in Huh7-dCas9-KRAB cells transiently
889 transfected with LIE sgRNAs and treated with 600 μM PA for 20 hours compared to vehicle-
890 treated controls (n = 3 per group). Molecular weigh in kDa for ladder noted. One way ANOVA
891 with multiple comparisons test was used to compare groups.
892 * $P < 0.05$, ** $P < 0.01$, *** $P < 0.001$.

Figure 4: In vivo repression of the murine hepatic LIE lowers CDAHFD-induced steatohepatitis.

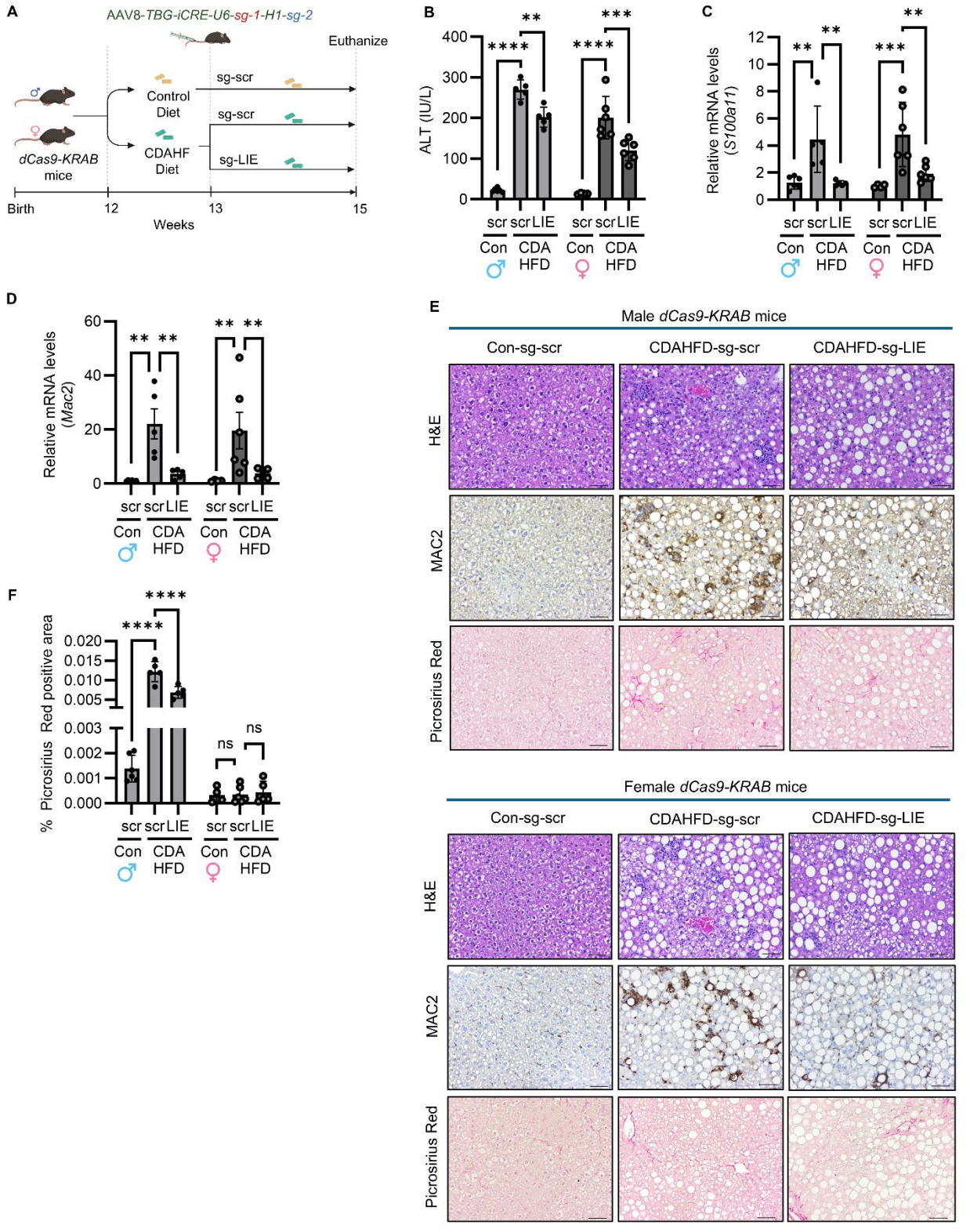

(A) Schematic depicts the CDAHF diet regimen for the *dCas9-KRAB* mice study. Male: Con-scramble (n = 6), CDAHFD-scramble (n = 5), CDAHFD-LIE (n = 5) and Female: Con-scramble (n = 4), CDAHFD-scramble (n = 6), CDAHFD-LIE (n = 6).

(B) Serum ALT levels in male and female mice. Male mice datapoints are represented as solid circles and female mice as gray circles. Two way ANOVA with multiple comparisons test was used to compare two groups with multiple conditions.

(C-D) Expression of **(C)** *S100a11* and **(D)** *Mac2* transcripts from the livers of AAV8-LIE injected CDAHFD-fed mice. Two way ANOVA with multiple comparisons test was used to compare two groups with multiple conditions.

(E) Histological assessments of the liver sections via H&E staining (top row), MAC2 (galectin 3) staining (middle row), and picrosirius red staining (bottom row) is demonstrated through representative images from evaluation of total number of samples as outlined in panel A. Scale bar: 50 μm.

(F) Area of the picrosirius red-positive collagen fibers per field were quantified using polarized microscopy. Each point represents one mouse with value averaged from 5 images (n = 4-6 mice per group). Two way ANOVA with multiple comparisons test was used to compare two groups with multiple conditions.

** $P < 0.01$, *** $P < 0.001$, **** $P < 0.0001$.

Figure 5: In vivo repression of the murine hepatic LIE lowers FFC diet-induced MASH.

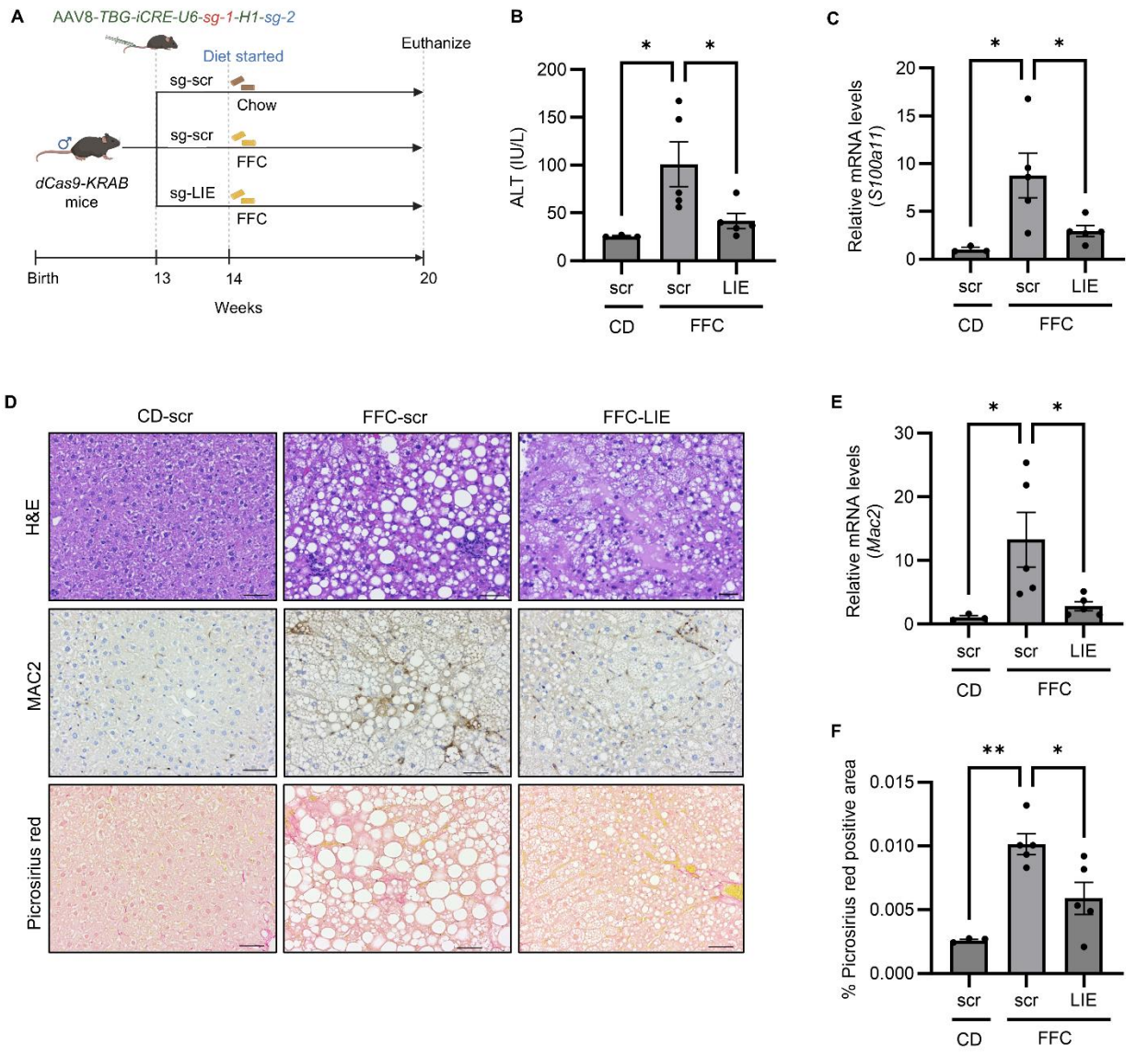

(A) Schematic depicting the FFC diet regimen for the *dCas9-KRAB* mice study. CD-scramble (n = 3), FFC-scramble (n = 5), FFC-LIE (n = 5).

(B) Serum ALT levels. One way ANOVA with Sidak multiple comparisons test was used to compare three conditions.

(C) Expression of *S100a11* transcript in the livers of AAV8-LIE injected FFC-fed mice compared to the AAV8-scr injected FFC control mice. One way ANOVA with Sidak multiple comparisons test was used to compare three conditions.

(D) Histological assessments of the liver sections via H&E staining (top row), MAC2 (galectin 3) staining (middle row), and picrosirius red staining (bottom row) is demonstrated through representative images from a total number of slides as indicated in panel A. Scale bar: 50 μm.

(E) Expression of *Mac2* transcripts in the livers of AAV8-LIE injected FFC-fed mice compared to the AAV8-scr injected FFC control mice. One way ANOVA with Sidak multiple comparisons test was used to compare three conditions.

(F) Area of the picrosirius red-positive collagen fibers in the liver sections were quantified using the polarized microscopy (n = 3-5 mice per group). Each point represents one mouse with values averaged from 5 images. One way ANOVA with Sidak multiple comparisons test was used to compare three conditions.

* $P < 0.05$, ** $P < 0.01$.